Nanoscale Advances

ROYAL SOCIETY OF CHEMISTRY

PAPER

View Article Online
View Journal | View Issue

Cite this: *Nanoscale Adv.*, 2026, **8**, 896

Two-dimensional Fe-MOF and bimetallic NiFe-MOFs with different Ni : Fe ratios for superior electrochemical performance in supercapacitor applications

Hanaa A. Mohamedien,[a] Abeer Enaiet Allah,[b] Soha M. Kamal[a] and Fatma Mohamed *[b]

Supercapacitors (SCs) are garnering significant attention owing to their remarkable power density. Transition-metal-based MOFs have abundant valence states, which contribute to their superior stability, high energy density, and high power density. In this study, monometallic Fe-BDC MOF and bimetallic NiFe-BDC MOFs were synthesized with different molar ratios and examined for their application in supercapacitors. SEM-coupled EDX, BET, and XRD analyses were performed to determine their morphologies and microstructures. The electrodes were evaluated through cyclic voltammetry (CV), galvanostatic charge/discharge (GCD), and electrochemical impedance spectroscopy (EIS) measurements in a 1 M KOH aqueous electrolyte. The $Ni_{10}Fe_1$-BDC MOF electrode exhibited the highest capacitance (918.75 F g^{-1}) at 4 A g^{-1} due to its fast ion transport and low electrical resistance, resulting from its spherical structure. The $Ni_{10}Fe_1$-BDC MOF//$Ni_{10}Fe_1$-BDC MOF symmetric supercapacitor accomplished a high energy density of 106.42 Wh kg^{-1} at a power density of 3720 W kg^{-1} and exhibited a high rate capability of 137.73% after 2000 cycles, indicating its potential in supercapacitor applications.

Received 15th March 2025
Accepted 25th November 2025

DOI: 10.1039/d5na00246j

rsc.li/nanoscale-advances

1 Introduction

Over the years, fossil fuels (for example, coal, natural gas, and petroleum oil) have been the sole source of energy for industrial and domestic purposes. However, currently, the world faces significant environmental issues due to the excessive usage of fossil fuels that depend on carbon and subsequently release greenhouse gases, mainly CO_2, which causes environmental pollution; therefore, the development of sustainable clean energy sources is an effective and particularly urgent solution to solve these issues.[1–3] Among the sustainable clean energy sources and devices, supercapacitors (SCs), also named ultra-capacitors or electrochemical capacitors, have prompted significant interest owing to their high long cyclic stability and coulombic efficiency and outstanding power density.[2,4] Electric double-layer capacitors (EDLCs), pseudo-capacitors (PCs), and battery-type capacitors (BTCs) are supercapacitor types in accordance with their energy storage mechanism.[5] PCs and BTCs offer higher specific capacities and energy densities than EDLCs due to the redox reactions of electrode materials' surface-active substances and faradaic charge transfer at electroactive sites' surfaces or reversible chemical interaction between electrode materials and ions of electrolyte in both PCs and BTCs, compared to the electrostatic physical charge transfer, without electrochemical reaction in EDLCs.[5]

Metal–organic frameworks (MOFs) are a type of porous inorganic–organic hybrid crystals composed of metal ions (clusters) bonded to organic linkers (ligands) through coordinate bonds. They have been used in different fields, such as sensors, catalysis, wastewater treatment, gas adsorption, biomedicine, drug delivery, water splitting, batteries, and supercapacitors, because of their fascinating characteristics.[6,7] MOFs are useful for electrochemical energy storage in supercapacitors due to their high surface area, possible pseudocapacitive redox centers, structural and functional flexibility, tunable pore size, and controllable micro-pore structures.[7] MOFs can be used as precursors to prepare other materials, such as metal oxides, metal nitrides, metal phosphides, carbon materials, or composites.[5]

Ni–Fe-based materials have drawn a lot of interest because of their high theoretical capacitance and promising electrocatalytic performance owing to the different oxidation states and the synergistic effect between Ni and Fe, which favors faradaic reactions that result in the enhanced electrochemical performance of the electrode active material.[8,9] Zhao *et al.* synthesized a $NiFe_2O_4$ material through a hydrothermal process, formed a paste on nickel foam (NF), and obtained a specific capacitance of ~100 F g^{-1} at a current density of

[a]*Applied Electrochemistry Laboratory, Chemistry Department, Faculty of Science, Beni-Suef University, 62511 Beni-Suef, Egypt*

[b]*Materials Science Lab, Chemistry Department, Faculty of Science, Beni-Suef University, Beni-Suef 62511, Egypt. E-mail: F_chem2010@yahoo.com*

1 A g^{-1}. In addition, they improved the specific capacitance of $NiFe_2O_4$ by fabricating the $Co_3O_4/NiFe_2O_4$ hybrid material, which attained a specific capacitance of ~225 F g^{-1} in a 3 M KOH electrolyte.[10] Kumar *et al.* prepared $Ni_{11.7}Fe_1$-LDH from NiFe-coordination polymer (NiFe-CPs) precursors and achieved a specific capacitance of 702 F g^{-1} at 0.25 A g^{-1} in a 3 M KOH electrolyte.[9] Choi and his group synthesized sulfur-doped nickel–iron nanostructures, S-doped NiFe-oxide nanoflowers (NFs) and macroparticles (MPs) *via* co-precipitation and hydrothermal-sulfurization approaches, respectively. They obtained specific capacitance values of 605 F g^{-1} for NiFeS-NFs and 515 F g^{-1} for NiFeS-MPs at 1 A g^{-1} in an aqueous 3 M KOH electrolyte using NF as the substrate.[11] Weng *et al.* synthesized NiFe-MOFs by a simple solvothermal approach directly on the NF substrate for different reaction times: 4, 8, and 12 h. They found that the best sample was NiFe-MOF-8, which offered 5964 mF cm^{-2}, the largest areal capacitance at 2 mA cm^{-2} in a potential window of 0–0.34 V in the presence of a 1 M KOH aqueous electrolyte.[4] Dong and his co-workers synthesized ultrathin nanosheets of NiFe-MOF through a one-step solvothermal method directly on an NF substrate using various molar ratios of Ni/Fe precursors. They obtained 11.0 F cm^{-2} (2750 F g^{-1}) capacitance at 5 mA cm^{-2} for the NiFe-MOF-3 : 2 sample in a 1 M KOH aqueous solution.[12] Nivetha *et al.* fabricated a NiFe-MOF by a simple solvothermal method, which exhibited a capacitance of 1190.88 F g^{-1} at 1 mV s^{-1} in a 2 M KOH electrolyte.[13] Zhang and his group prepared a NiFe-MOF using benzene tricarboxylic acid as the organic linker through a solvothermal method on an NF substrate, obtaining ~450 F g^{-1} capacitance at 0.5 A g^{-1} current density. They improved the specific capacitance of NiFe-MOF through the fabrication of NiFe-MOF@NiFeTe composites using different amounts of Na_2TeO_3 as the Te source; NiFe-MOF@NiFeTe-2 delivered ~1650 F g^{-1} capacitance at 0.5 A g^{-1} in a 1 M KOH solution.[14] Patil *et al.* prepared MOF-derived $NiFe_2O_4$ at different annealing temperatures (460, 500, and 550 °C) for 6 h, prepared the working electrode using a homogeneous slurry on a stainless steel (SS) substrate, and obtained the highest capacitance of 833 F g^{-1} at 0.25 A g^{-1} for the MOF-derived NFO500 sample in 1 M KOH.[15] Zhang *et al.* synthesized NiFe-LDH with different Ni : Fe molar ratios *via* a hydrothermal method. They fabricated the working electrode in the form of a viscous paste on NF and obtained the highest capacity of 114.4 mA h g^{-1} for the Ni_5Fe_1-LDH sample in a 6 M KOH solution.[16]

Bimetallic MOFs can give higher theoretical capacitance than single metallic MOFs because of the synergistic effects of the two metal cations and more abundant redox active sites, which improve the electronic conductivity and charge storage ability.[2,12,17] Moreover, bimetallic MOFs exhibit better cycle stability than single metallic MOFs.[12] In addition, MOFs based on Ni, Co, and Fe can be employed as bifunctional electrode materials due to the presence of d-band electrons and abundant valence changes. Moreover, MOFs synthesized without additional annealing are still not commonly used as electrode materials in supercapacitors (SCs), water electrolysis, and electrochemical sensing.[4]

Herein, we fabricated a series of Fe-BDC MOF and NiFe-BDC MOFs in different precursor ratios through a simple solvothermal method without any complicated or energy-consuming processes like annealing, and they were employed as promising materials for supercapacitor applications. The results reveal that the optimized NiFe-BDC MOF exhibited a high specific areal capacitance along with good cycle stability. Our work reveals that the study of bimetallic MOFs which have strong coordination ability is an effective strategy to enhance the cycle stability of MOFs along with boosting the specific capacitance.

2 Experimental section

2.1. Materials and chemicals

Iron nitrate nonahydrate ($Fe(NO_3)_3 \cdot 9H_2O$) was acquired from Sigma-Aldrich; nickel chloride hexahydrate ($NiCl_2 \cdot 6H_2O$) was bought from LOBA Chemie; benzene dicarboxylic acid (BDC) was obtained from Central Drug House (P) Ltd; *N*,*N*-dimethyl formamide (DMF) was purchased from CARLO ERBA; ethanol and potassium hydroxide pellets (KOH) were purchased from ISOLAB chemicals; the Nafion-117 solution was purchased from Sigma-Aldrich.

2.2. Synthesis of NiFe-BDC MOF

The NiFe-BDC MOFs were synthesized using a simple solvothermal method. First, 2.73 mmol $NiCl_2 \cdot 6H_2O$ and 0.27 mmol $Fe(NO_3)_3 \cdot 9H_2O$ (at an Ni : Fe molar ratio 10 : 1) were dissolved in 10 mL *N*,*N*-dimethyl formamide (DMF) individually, stirred, then mixed with each other under stirring for 10 min to form solution A. Then, 3 mmol benzene dicarboxylic acid (BDC) was dissolved in 20 mL DMF and stirred for 10 min to form solution B. Next, solution B was added to the mixed solution of metal salts (solution A) dropwise, stirred for 10 min, and then ultrasonicated for 60 min at ambient temperature. Finally, the mixture was transferred into a 60 mL stainless steel autoclaved kettle lined with Teflon for 22 h at 150 °C. The obtained sample was collected through filter paper, washed three times using DMF and dissolved in methanol under stirring for 1 h. Finally, the precipitate was dried at 80 °C overnight. Moreover, NiFe-BDC MOFs with different Ni : Fe precursor molar ratios (0 : 1, 5 : 1, 15 : 1, and 20 : 1) were also synthesized using the same experimental procedure and named Fe-BDC MOF, Ni_5Fe_1-BDC MOF, $Ni_{15}Fe_1$-BDC MOF, and $Ni_{20}Fe_1$-BDC MOF, respectively. The total molar amount of metal ions was kept a constant.

2.3. Characterization

The morphologies of the prepared materials were characterized using scanning electron microscopy (SEM, JEOL Ltd, JSM-IT200, Tokyo, Japan). In addition, the elemental compositions were examined using EDX coupled with SEM. Powder X-ray diffraction (PXRD) was performed on an X-ray diffractometer (JSX-60PA, Japan) using Cu Kα radiation with a wavelength of 1.5418 Å for examining the crystalline structure of the prepared substances. The surface areas and pore-size distributions of the samples were studied using the Brunauer–Emmett–Teller (BET) method based on N_2 adsorption–desorption isotherms recorded on a Tri-Star II 3020 (Micromeritics, USA) analyzer.

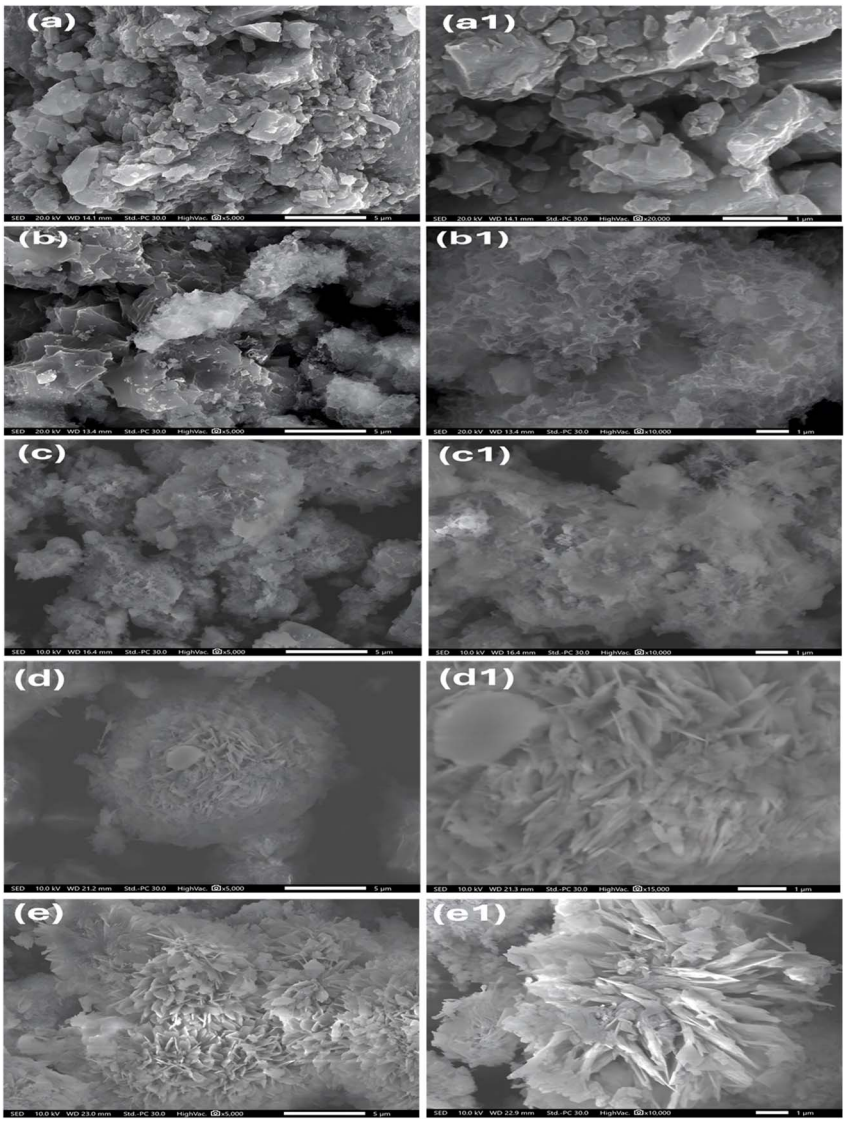

Fig. 1 SEM images of the (a and a1) Fe-BDC MOF, (b and b1) Ni_5Fe_1-BDC MOF, (c and c1) $Ni_{10}Fe_1$-BDC MOF, (d and d1) $Ni_{15}Fe_1$-BDC MOF, and (e and e1) $Ni_{20}Fe_1$-BDC MOF materials at different magnifications.

2.4. Electrochemical measurements

The electrochemical measurements of the prepared samples were carried out using a three-electrode setup, in which a platinum wire was the counter electrode, Ag/AgCl was used as the reference electrode, and a graphite sheet was the working electrode (WE) in a 1 M KOH electrolyte. The WE (graphite sheet current collector) had a 1 cm^2 active surface area and was prepared by dispersing 1 mg of the prepared materials in 200 μL of a mixed solvent of 1 : 2 (v/v) isopropanol/water (comprising 10 μL Nafion-117 solution) under sonication at ambient temperature to form a homogenous ink, which was dropped onto the graphite WE and dried at a temperature of 60 °C. A potentiostat/galvanostat (AUTOLAB PGSTAT 302N, Metrohm, Switzerland) with NOVA 1.11 software was employed to perform all the electrochemical measurements. The electrochemical performance of the as-prepared electrodes was explored by cyclic voltammetry (CV) and galvanostatic charge–discharge (GCD) methods in a voltage range of −0.4 to 0.6 V for CV and −0.2 to 0.5 V for GCD. A frequency range of 0.01 Hz to 100 kHz was used for electrochemical impedance spectroscopy (EIS) measurements at an AC amplitude of 10 mV.

The specific capacitances of the electrodes were estimated from the CV curves using eqn (1):[18–20]

$$C_s = (\int i\mathrm{d}V)/(2mv\Delta V) \quad (1)$$

where C_s is the specific capacitance (F g^{-1}), $\int i\mathrm{d}V$ is the integrated area of the CV curve (AV), m is the active material mass (g), v is the scan rate (V s^{-1}), and ΔV is the potential window (V).

The gravimetric specific capacitance (C_s), areal capacitance (C_A), and specific capacity (Q_s) of the as-prepared electrodes were computed from the GCD curves using eqn (2)–(4), respectively:[18,21,22]

$$C_s = (It)/(m\Delta V) \quad (2)$$

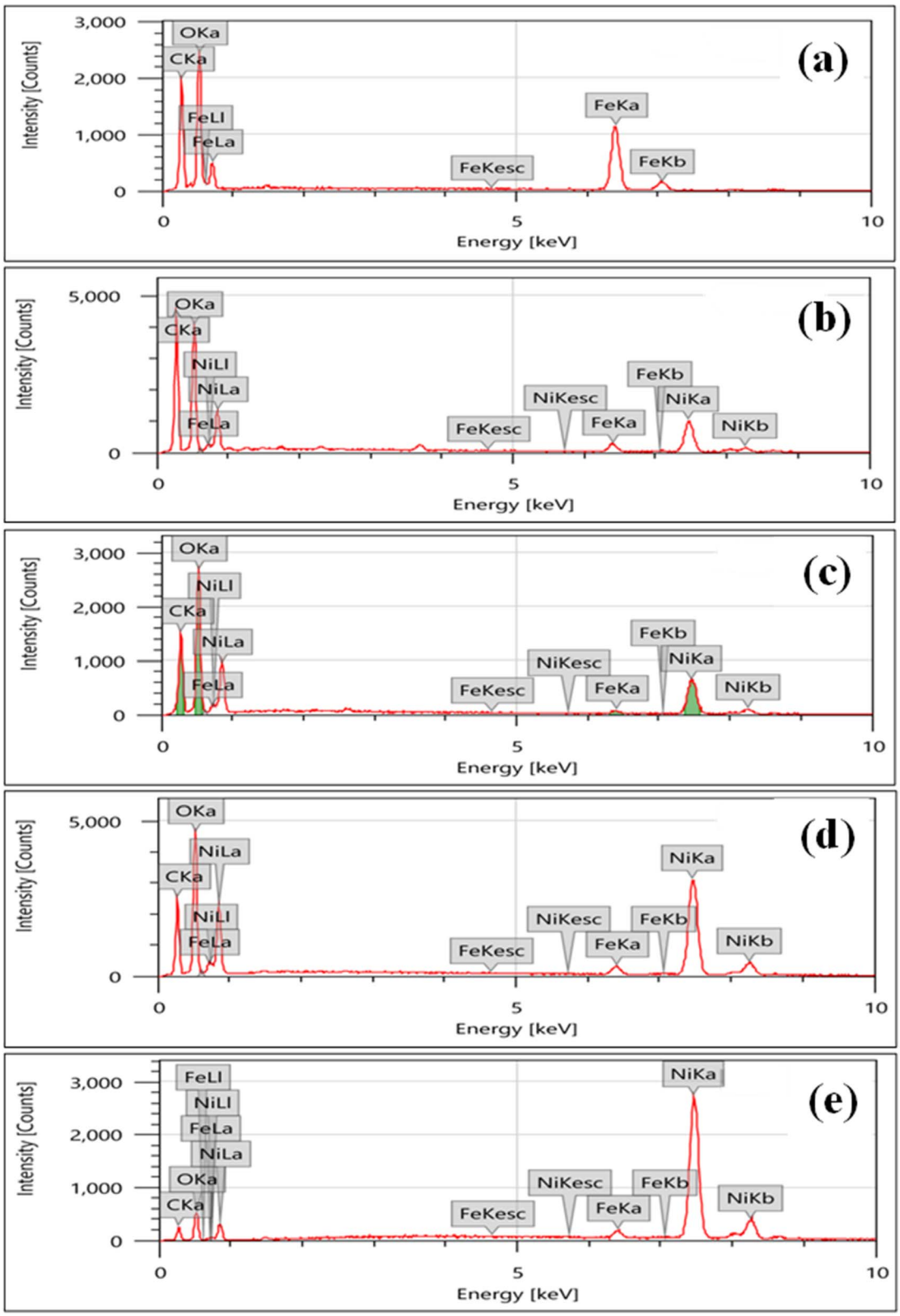

Fig. 2 EDX spectra of the (a) Fe-BDC MOF, (b) Ni_5Fe_1-BDC MOF, (c) $Ni_{10}Fe_1$-BDC MOF, (d) $Ni_{15}Fe_1$-BDC MOF, and (e) $Ni_{20}Fe_1$-BDC MOF materials.

Table 1 Atomic percentages of the constituent elements of Fe-BDC MOF and NiFe-BDC MOFs obtained from the EDX analysis

Material	Element composition (at%)			
	Ni	Fe	C	O
Fe-BDC MOF	—	4.08	49.61	46.31
Ni_5Fe_1-BDC MOF	2.41	0.39	54.42	42.78
$Ni_{10}Fe_1$-BDC MOF	6.92	0.29	47.33	45.46
$Ni_{15}Fe_1$-BDC MOF	8.43	0.40	47.52	43.64
$Ni_{20}Fe_1$-BDC MOF	38.43	0.98	39.63	20.96

$$C_A = (It)/(A\Delta V) \quad (3)$$

$$Q_s = It/m \quad (4)$$

where C_s is the gravimetric specific capacitance (F g^{-1}), C_A is the areal capacitance (F cm^{-1}), Q_s is the specific capacity (C g^{-1}), I is the current (A), the discharge time is t (s), m is the active material mass (g), the potential change during the discharge process (V) (excluding the IR drop) is ΔV and A is electrode active area (cm^2).

2.4.1. Two-electrode system. The symmetrical supercapacitor was fabricated with a two-electrode configuration using two identical $Ni_{10}Fe_1$-BDC MOF electrodes in a 1 M KOH aqueous electrolyte. The working electrodes were prepared using the same procedure as those in the three-electrode system. 1 mg of $Ni_{10}Fe_1$-BDC MOF was dispersed in 200 μL of a mixed solvent of 1 : 2 (v/v) isopropanol/water (containing 10 μL Nafion-117 solution) and drop-casted on each graphite sheet with an active area of 1 × 1 cm^2. The specific capacitance of the symmetric cell was computed using eqn (5). The specific capacitance (C_s, F g^{-1}) of a single electrode was calculated from the CV data using eqn (5) or (6).[20,23] In addition, the gravimetric specific capacitance (C_s, F g^{-1}) from the GCD data was calculated using eqn (7) or (8),[20,23–28] while the specific capacity (Q_s) was calculated using eqn (9). The energy density (E) and power density (P) were estimated according to eqn (10) and (11), respectively.[23,26,27]

$$C_s = 4C_{cell} = 4(\int I dV)/(2Mv\Delta V) \quad (5)$$

$$C_s = (\int I dV)/(mv\Delta V) \quad (6)$$

$$C_s = 4C_{cell} = 4(It)/(M\Delta V) \quad (7)$$

$$C_s = 2(It)/(m\Delta V) \quad (8)$$

$$Q_s = 4It/M = 2It/m \quad (9)$$

$$E = (C_s\Delta V^2)/(2 \times 3.6) \quad (10)$$

$$P = 3600E/\Delta t \quad (11)$$

where C_{cell} is the specific capacitance of the cell (F g^{-1}), C_s is the specific capacitance of the single electrode (F g^{-1}), I is the current (A), t is the discharge time (s), M is the combined mass of the two electrode-active substances (g), which equals 2 m as the mass of both electrodes are the same in the symmetric supercapacitor cell, m is the active material mass of single electrode (g), ΔV is the potential variation during the discharge process (V) (excluding the IR drop), E stands for energy density (Wh kg^{-1}) and P stands for power density (W kg^{-1}).

3 Results and discussion

3.1. Structural characterization

3.1.1. Scanning electron microscopy (SEM). The microstructure and morphology of the prepared samples were characterized using scanning electron microscopy (SEM) at different magnifications. The Fe-BDC MOF (Fig. 1a and a1) consisted of layer-by-layer stacking of flakes that formed large particles. However, the incorporation of Ni to form bimetallic MOFs changed the morphology of the two-dimensional structure of the Fe-BDC MOF particles, as displayed in Fig. 1b–e1. The NiFe-BDC MOFs consisted of interwoven reticular nanosheets or fibers that were notably thinner and placed in closer positions, resulting in an increase in the growth rate of the NiFe-MOFs

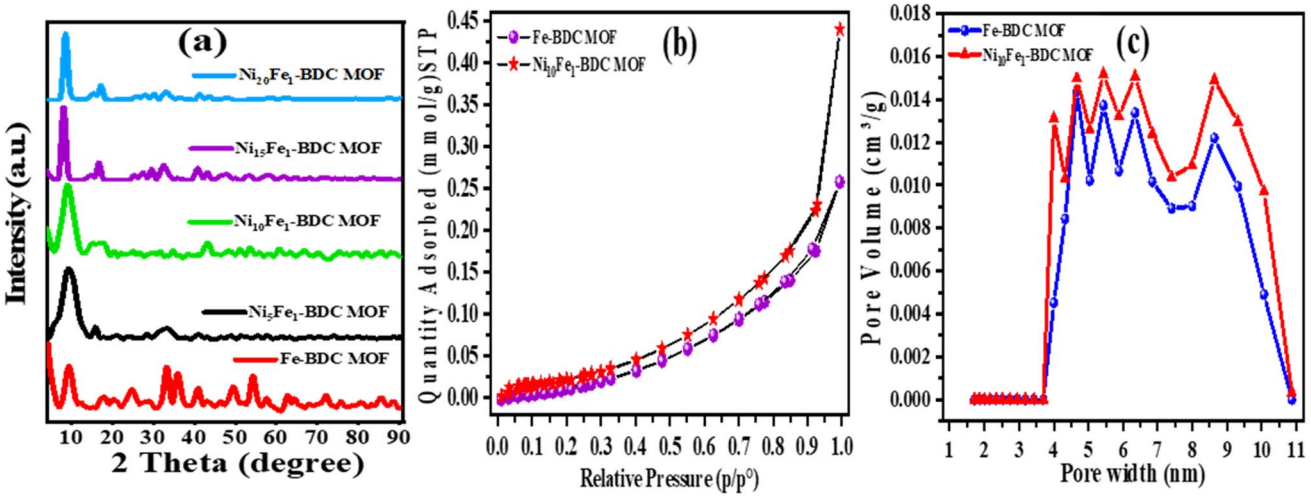

Fig. 3 (a) XRD patterns of the Fe-BDC MOF and NiFe-BDC MOF materials with different Ni : Fe ratios. (b) N_2 adsorption–desorption isotherms and (c) pore size distributions of the Fe-BDC MOF and $Ni_{10}Fe_1$-BDC MOF materials.

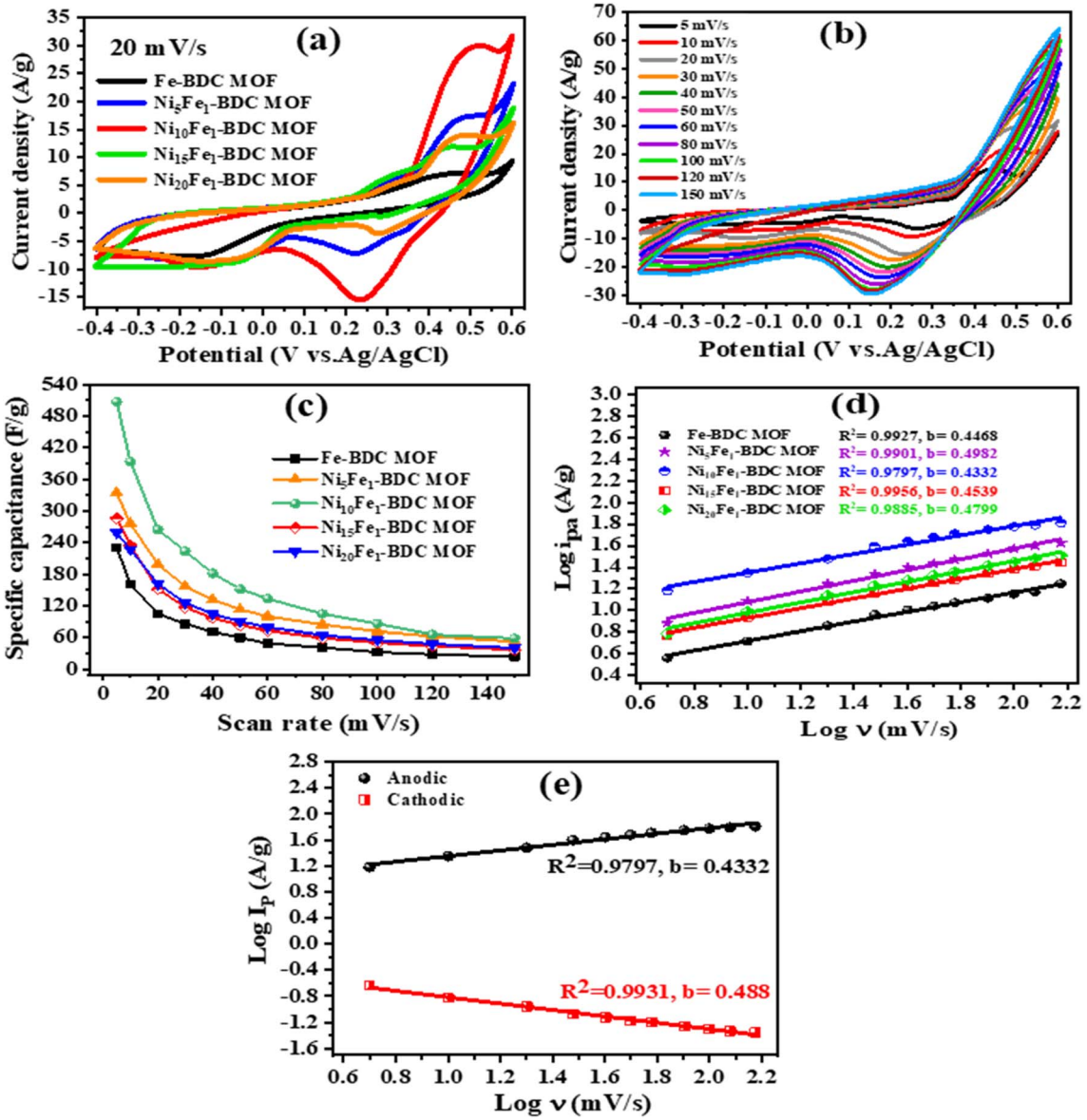

Fig. 4 Cyclic voltammetry (CV) measurements. (a) CV curves of all the fabricated electrode materials at 20 mV s^{-1}, (b) CV of the $Ni_{10}Fe_1$-BDC MOF electrode at different scan rates, (c) specific capacitance (F g^{-1}) of all the electrodes measured as a function of the scan rate, (d) logarithmic plots of anodic peak current density (log i_{pa}) *versus* scan rate (log ν) of the Fe-BDC MOF and different NiFe-BDC MOF electrodes, and (e) logarithmic relationship between the anodic and cathodic peak current densities (log i_p) of the $Ni_{10}Fe_1$-BDC MOF electrode at different scan rates (log ν).

with increasing Ni^{2+} content. Furthermore, the morphology completely changed to a flower-like structure with increasing nickel ion concentrations. The flower consisted of nanosheets that were vertically aligned and crossed each other, leading to the formation of gaps between them and also among individual petals, signifying electrolyte accessibility several routes for easy ion transport and electron transfer, thus enhancing the electrochemical performance of the materials for energy storage device applications. The distinctive nanostructures ensure sufficient space between the nanosheets, which improves electrolyte ion adsorption and desorption during the charge/discharge process and allows the maximum utilization of active materials, hence increasing the charge storage capacity. Furthermore, the EDX analysis was performed to validate the specific elemental compositions of the five studied electrode materials, as demonstrated in Fig. 2. The analysis results imply that the sample Fe-BDC MOF (Fig. 2a) was composed of C, O and Fe, while the other NiFe-BDC MOFs materials were composed of C, O, Fe and Ni elements at different atomic percents, as shown in Table 1.

3.1.2. Powder X-ray diffraction. The catalyst compositions were investigated by powder X-ray diffraction. The XRD patterns of Fe-BDC MOF and NiFe-BDC MOFs are shown in Fig. 3. The Fe-BDC MOF crystal structure could not be correctly identified. It is often difficult to identify the crystalline phase of MOFs based on iron and terephthalic acid ligand, as they can

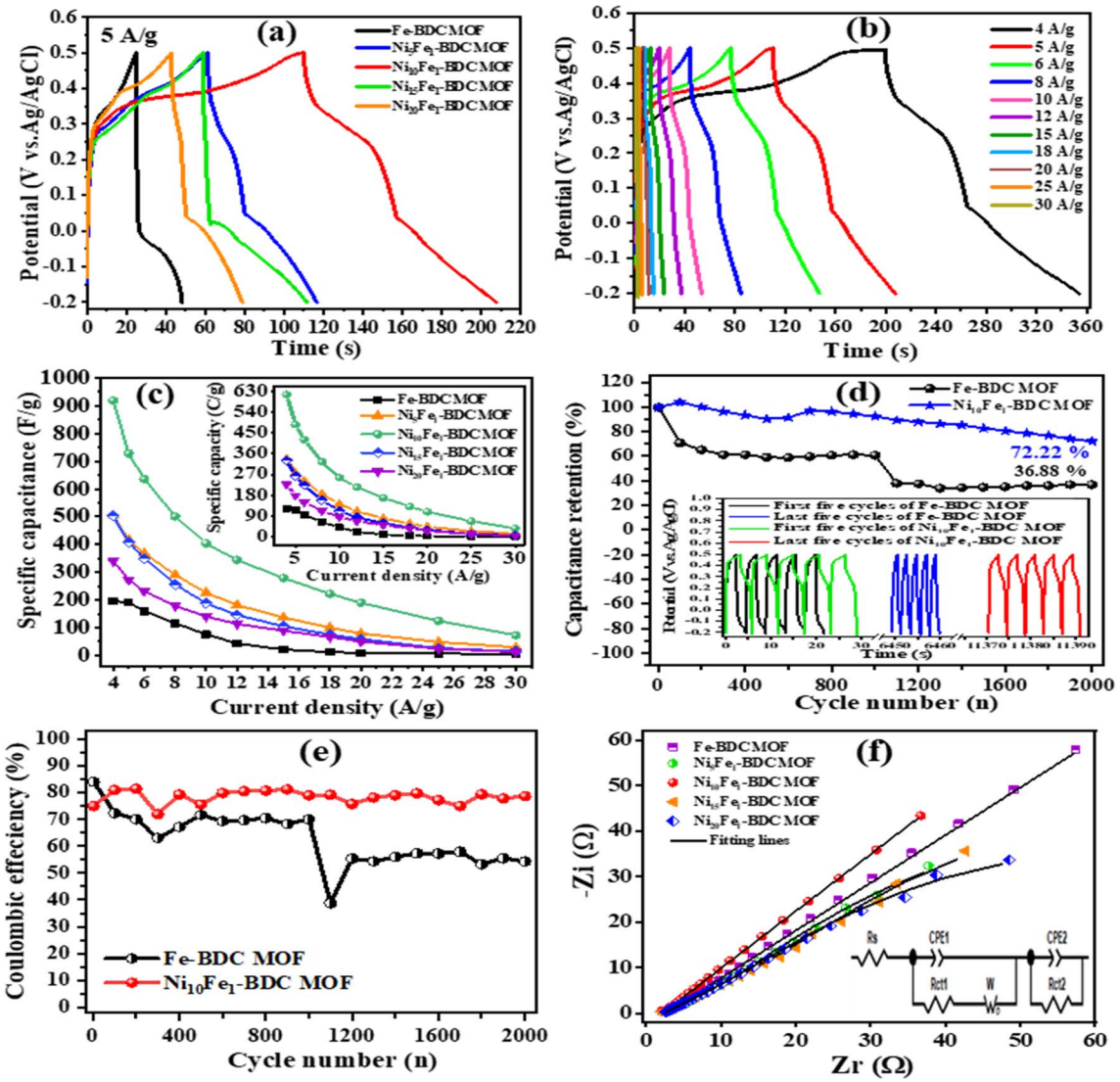

Fig. 5 (a) Galvanostatic charge–discharge (GCD) curves of all the fabricated electrode materials at a current density of 5 A g^{-1}, (b) GCD curves of the Ni_{10}–Fe_1 BDC MOF electrode at different current densities, (c) specific capacitance (F g^{-1}) and specific capacity (C g^{-1}) of Fe-BDC MOF and NiFe-BDC MOFs *versus* different current densities, (d) cycling stability of the Fe-BDC MOF and $Ni_{10}Fe_1$-BDC MOF electrodes at 12 A g^{-1} for 2000 GCD cycles, (e) coulombic efficiency of the Fe-BDC MOF and $Ni_{10}Fe_1$-BDC MOF electrodes at 12 A g^{-1} for 2000 cycles, and (f) Nyquist plots of Fe-BDC MOF and NiFe-BDC MOFs (the inset shows the equivalent circuit diagram).

crystallize in a variety of ways according to the synthesis conditions (temperature, time, solvent polarity, *etc.*).[29,30] The Fe-BDC MOF sample showed characteristic peaks located at 2θ = 9.4°, 12°, 18.2°, 20.2°, 24.8°, and 29°, related to (002), (101), (103), (200), (202), and (211) planes, respectively.[31,32] Furthermore, the peaks present at 33.2°, 36°, 41°, 49.4°, 54.2°, 57.6°, 62.8°, 64.4°, 72.2° and 75.6° and attributed to (104), (110), (113), (024), (116), (018), (214), (030), (620) and (622) planes, respectively, could be assigned to hematite (Fe_2O_3) and/or magnetite (Fe_3O_4).[29,33,34] After the addition of Ni, the crystallinity of the NiFe-MOFs increased compared with that of the Fe-BDC MOF. They showed a characteristic peak at 9.2° related to the (100) plane, which demonstrated that the NiFe-BDC MOF was successfully synthesized (JCPDS no. 35-1677).[35,36] Moreover, the intensity of this peak in the $Ni_{20}Fe_1$-BDC MOF sample was higher than those of $Ni_{15}Fe_1$-BDC MOF and other samples, indicating an increase in the concentration of nickel due to the addition of more nickel salt. The PXRD patterns of the NiFe-BDC MOFs were similar to those reported in the literature.[12–14,37] The peak at 2θ = 17° matched with simulated MOF@DMF (CCDC no. 613596).[12] Furthermore, the peaks located at 2θ = 33°, 41° agree with those previously reported for NiFe-BDC MOF.[14] The prepared $Ni_{10}Fe_1$-BDC MOF material showed the lowest crystallinity among the prepared NiFe-BDC MOFs, indicating an amorphous structure, which facilitates the diffusion of electrolyte ions; thus, its electrochemical performance is the highest among the prepared samples.[12]

3.1.3. Brunauer–Emmett–Teller (BET) analysis. Nitrogen adsorption and desorption isotherms were used to evaluate the

BET surface area and pore size distributions of the synthesized Fe-BDC MOF and $Ni_{10}Fe_1$-BDC MOF materials.

The N_2 adsorption/desorption isotherm measurements revealed how surface area and porosity changed from Fe-BDC MOF to $Ni_{10}Fe_1$-BDC MOF materials. As displayed in Fig. 3b, both samples exhibited typical type-IV hysteresis loops, verifying the mesoporous structure of both samples with mesopores in the 2–50 nm diameter range.[25,38,39] The pore size distribution curves in Fig. 3c also prove the above results. Furthermore, the pristine Fe-BDC MOF material showed a specific surface area of 1.9621 $m^2\ g^{-1}$, a pore volume of 0.008805 $cm^3\ g^{-1}$, and a pore size of 179.5058 Å, which were smaller than those of $Ni_{10}Fe_1$-BDC MOF (2.2965 $m^2\ g^{-1}$, 0.014827 $cm^3\ g^{-1}$, and 258.2522 Å, respectively). The increase in surface area and porosity in $Ni_{10}Fe_1$-BDC MOF provides more active sites and sufficient space for electron transfer and accessible transportation bridges for ion diffusion, hence improving the electrochemical performance. The distribution of pore size was calculated from the branch of adsorption. Fig. 3c reveals the presence of mesopores with diameters of 4.66, 5.43, 6.34, and 8.63 nm in Fe-BDC MOF, as well as pores with diameters of 4, 4.66, 5.43, 6.34, and 8.63 nm in $Ni_{10}Fe_1$-BDC MOF.

Fig. S1a shows that the three samples exhibited typical type-IV hysteresis loops, verifying their mesoporous structure (mesopores with 2–50 nm diameter). The pore size distribution curves in Fig. S1b also prove the above results. Furthermore, the specific surface areas were 16.9784 $m^2\ g^{-1}$, 26.8457 $m^2\ g^{-1}$, and 34.6821 $m^2\ g^{-1}$, while the pore volumes were 0.079477 $cm^3\ g^{-1}$, 0.080370 $cm^3\ g^{-1}$, and 0.112733 $cm^3\ g^{-1}$, and the pore sizes were 187.2438 Å, 119.7510 Å, and 130.0190 Å for Ni_5Fe_1-BDC MOF, $Ni_{15}Fe_1$-BDC MOF, and $Ni_{20}Fe_1$-BDC MOF materials, respectively.

3.2. Electrochemical performance studies

3.2.1. Three-electrode electrochemical performance study. The electrochemical performance of the as-prepared Fe-BDC MOF, Ni_5Fe_1-BDC MOF, $Ni_{10}Fe_1$-BDC MOF, $Ni_{15}Fe_1$-BDC MOF, and $Ni_{20}Fe_1$-BDC MOF electrodes was studied in a three-electrode configuration using cyclic voltammetry (CV), galvanostatic charge–discharge (GCD), and electrochemical impedance spectroscopy (EIS) tests in a 1 M KOH aqueous electrolyte. Fig. 4a displays the CV curves of the studied electrodes at a scan rate of 20 mV s^{-1} in a −0.4 to 0.6 V potential window; all CV curves display a pair of redox peaks originating from the faradaic redox reactions between Fe^{2+}/Fe^{3+} and Ni^{2+}/Ni^{3+}, indicating the redox behavior and faradaic battery-type features of the materials. The enhancement of the integrated CV areas of the NiFe-BDC MOF samples compared with that of the Fe-BDC MOF is most likely because of the synergistic effect of the Ni and Fe, which aids in the battery-type performance of the NiFe-BDC MOFs. In addition, the CV integral area and peak current response of the $Ni_{10}Fe_1$-BDC MOF sample were the largest among the NiFe-BDC MOF materials, suggesting the highest electrochemical performance, which was additionally verified by the longest discharge time observed in the galvanostatic charge/discharge (GCD) curves. The CV curves of the $Ni_{10}Fe_1$-BDC MOF electrode at different scan rates are detailed in Fig. 4b. Upon increasing the scan rate from 5 to 150 mV s^{-1}, the peak currents and the integrated area increase, indicating the sufficiently fast transfer rates of electrons and ions because of the reversible redox reactions between the electrode and the electrolyte. Moreover, the anodic peaks shift towards more positive voltages, while the cathodic peaks move to negative potentials, signifying the electrode's polarization effect and the fast charge/discharge rate of the electrode materials' redox reversibility. The diffusion-controlled battery-type behavior of all studied materials is proven by the disappearance of the oxidation peak at high scan rates.[40] The CV curves of other measured electrodes also displayed similar results and are represented in Fig. S2. The probable electrochemical reactions are as follows:[41]

$$Ni^{2+} + 2OH^- \rightarrow Ni(OH)_2 \quad (12)$$

$$Ni(OH)_2 + OH^- \rightarrow Ni(OOH) + H_2O + e^- \quad (13)$$

$$Fe^{2+} + 2OH^- \rightarrow Fe(OH)_2 \quad (14)$$

$$Fe(OH)_2 + OH^- \rightarrow Fe(OOH) + H_2O + e^- \quad (15)$$

Fig. 4c represents the specific capacitance of all measured electrodes at different scan rates. It is obvious that the NiFe-BDC MOFs had a specific capacitance higher than that of the Fe-BDC MOF, indicating the synergistic effect between Ni and Fe. In addition, the $Ni_{10}Fe_1$-BDC MOF electrode showed the highest capacitance among the NiFe-BDC MOFs. Moreover, with increasing scan rates, the capacitance decreased owing to the lack of time for the electrolyte ions to enter deep into the inner layers of the electrodes at high scan rates; therefore, only the outer active surface is involved in the redox reactions.

With the aim of analyzing the mechanism of charge storage, the relationship between the current density (i, A g^{-1}) and scan rate (ν, mV s^{-1}) was evaluated using the following equation:[42,43]

$$i = a\nu^b \quad (16)$$

$$\log i = \log a + b \log \nu \quad (17)$$

where a and b are constants. Particularly, diffusion regulates charge storage when b is equal to 0.5. On the other hand, the surface capacitance mostly controls charge storage when b equals 1. In addition, when the b value is between 0.5 and 1, both diffusion and surface capacitance regulate charge storage. Logarithmic calculations based on the cathodic currents of the studied electrodes are illustrated in Fig. 4d. The b values were obtained from the slope of the linearly fitted $\log i$ *versus* $\log \nu$ curves. The figure illustrates that b values calculated from the anodic peak current of all studied electrodes are less than 0.5 ($b < 0.5$), suggesting that the charge storage is dominated by diffusion control, as indicated by the linearity of the graphs.[44] Fig. 4e displays the data analysis of the $Ni_{10}Fe_1$-BDC MOF electrode's anodic and cathodic peaks. The anodic and cathodic b-values are 0.4332 and 0.488, respectively, which indicate that

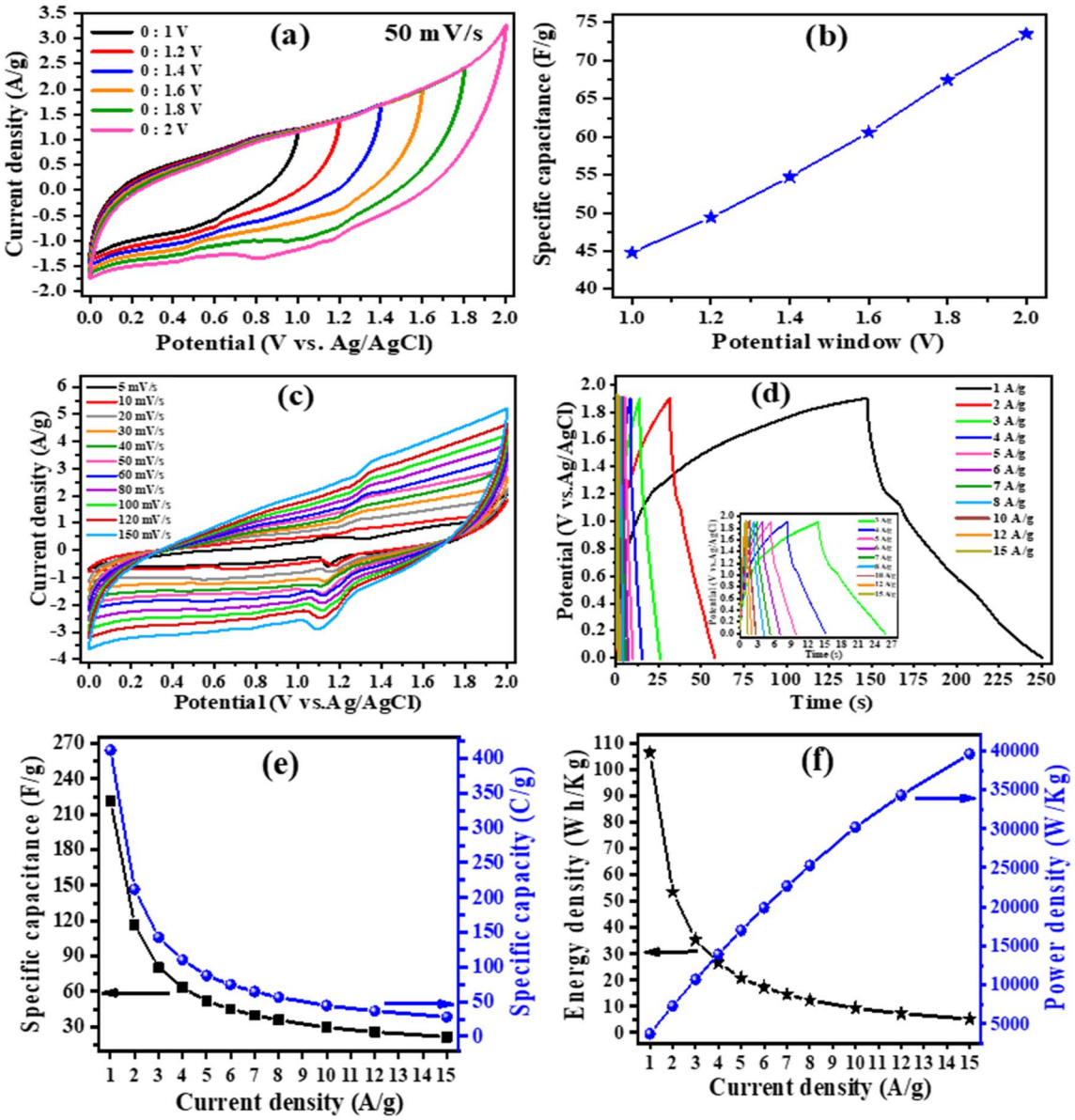

Fig. 6 Electrochemical performance of the symmetric supercapacitor cell (SSC): (a) CV curves at different potential windows measured at a scan rate of 50 mV s^{-1}, (b) specific capacitance (F g^{-1}) as a function of the potential window, (c) CV curves in the potential range of 0–2 V at different scan rates, (d) GCD curves measured at different current densities, (e) specific capacitance and capacity *versus* current density, and (f) energy density and power density at different current densities.

the energy storage mechanism is a diffusion-controlled process, which also matches with the disappearance of the oxidation peak at high scan rates.[40]

The galvanostatic charge–discharge (GCD) method was employed to determine the specific capacitance of the as-prepared electrodes at different current densities and within a potential range of −0.2 to 0.5 V. Fig. 5a displays a comparison of the GCD curves of the five studied samples at 5 A g^{-1} current density; the $Ni_{10}Fe_1$-BDC MOF electrode has the longest discharge time among the electrodes, suggesting its highest specific capacitance. The GCD curves display nonlinear behavior, which confirms the redox peaks present in the CV curves. Nickel (Ni) has a significant effect on the supercapacitor performance; therefore, as the Ni content increases, the specific capacitance of the NiFe-BDC MOFs increases because of the better redox behavior of Ni rather than Fe. Furthermore, the $Ni_{10}Fe_1$-BDC MOF has a superior amorphous structure over other samples, allowing for improved electrolyte ion intercalation and deintercalation and hence resulting in the highest specific capacitance. However, in the samples with higher content of Ni, the capacitance decreases because of increasing crystallinity, which affects electrolyte ion diffusion and, in turn, hampers the electrochemical performance.[12]

As shown in Fig. 5b, the GCD graphs of the Ni_{10}–Fe_1 BDC MOF electrode displayed a nonlinear behaviour. Additionally, the discharge time decreased as the current density increased

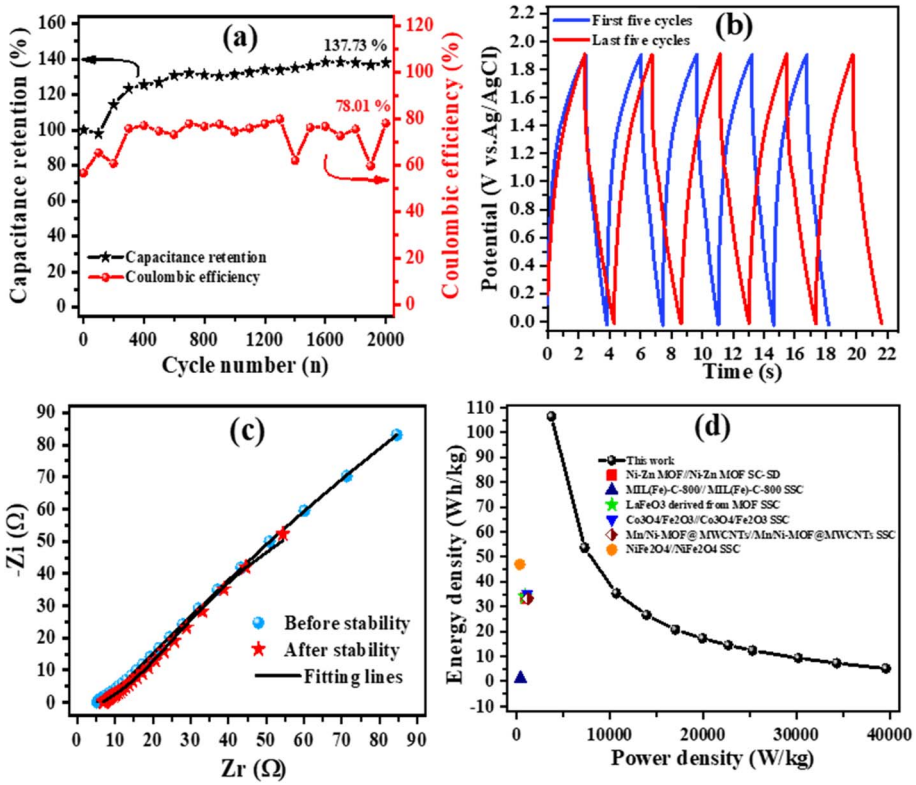

Fig. 7 (a) Cycling stability performance and coulombic efficiency of the symmetric supercapacitor cell at 8 A g^{-1}, (b) first and last five GCD cycles of the symmetric supercapacitor cell at 8 A g^{-1}, (c) electrochemical impedance spectroscopy (EIS) before and after the stability test, and (d) Ragone plot of the $Ni_{10}Fe_1$-BDC MOF//$Ni_{10}Fe_1$-BDC MOF symmetric supercapacitor cell.

because of the inadequate faradaic reaction of the active materials in a limited time (lack of time for the occurrence of redox reactions), enlarged resistance, and the involvement of only the outer active surface of the electrode in the redox reaction at elevated current densities.[45] The GCD graphs of the other electrode materials at different current densities are displayed in Fig. S3. Fig. 5c shows the specific capacitances and capacities estimated from the GCD curves of the samples at different current densities using eqn (2) and (4), respectively. The Ni_{10}–Fe_1 BDC MOF electrode gave the highest specific capacitance of 918.75 F g^{-1} (615.56 C g^{-1}) in contrast to 503.28 F g^{-1} (337.2 C g^{-1}) for the Ni_5–Fe_1 BDC MOF electrode, 503.25 F g^{-1} (331.64 C g^{-1}) for the Ni_{15}–Fe_1 BDC MOF electrode, 340.99 F g^{-1} (226.76 C g^{-1}) for the Ni_{20}–Fe_1 BDC MOF electrode, and 196.24 F g^{-1} (123.04 C g^{-1}) for the Fe-BDC MOF electrode at 4 A g^{-1} current density. Moreover, the capacitance and capacity decreased with increasing current density because of the involvement of only the outer active surface of the electrode in the redox reactions at elevated current densities. The superior capacity of the Ni_{10}–Fe_1 BDC MOF is due to the synergistic effect and the optimal ratio of Ni and Fe ions, and its amorphous structure.

The cycling stability of the synthesized Fe-BDC MOF and $Ni_{10}Fe_1$-BDC MOF materials was analyzed in a three-electrode system for 2000 GCD cycles at 12 A g^{-1} current density in a 1 M KOH electrolyte, as displayed in Fig. 5d; the inset of the figure is the first and last five cycles of the Fe-BDC MOF and $Ni_{10}Fe_1$-BDC MOF materials. 72.22% of the initial capacitance of $Ni_{10}Fe_1$-BDC MOF electrode was retained after 2000 GCD cycles, which is superior to that of the Fe-BDC MOF electrode (36.88%). The initial increase in the capacitance of the $Ni_{10}Fe_1$-BDC MOF electrode is related to the exposure of active sites to the electrolyte ions with rising cycle numbers, while the initial decrease in the capacitance of the Fe-BDC MOF electrode is ascribed to the structural destruction and instability.[46] In addition, the shape of the last 5 cycles of the $Ni_{10}Fe_1$-BDC MOF remained almost the same compared with that of the first 5 cycles, indicating exceptional electrochemical performance due to the presence of both Ni and Fe species, which contribute synergistically and provide multiple valence states. Furthermore, after 2000 GCD cycles, the coulombic efficiency of $Ni_{10}Fe_1$-BDC MOF was maintained at 78.7%, which was better than that of the Fe-BDC MOF electrode (54.35%), as presented in Fig. 5e. A comparison of the specific capacitances, electrolytes, cyclic stabilities, and morphologies of the Ni–Fe BDC MOF electrode with those of the previously reported three-electrode systems are presented in Table S1.

The electrochemical properties and resistance of the studied electrodes were examined using electrochemical impedance spectroscopy (EIS). Fig. 5f demonstrates the Nyquist plots, and the inset gives the equivalent circuit (EC) used to fit the EIS spectra to measure parameters, such as internal resistance (R_s), charge transfer resistance (R_{ct}), constant phase element (CPE), and Warburg impedance (W). Generally. Similar shapes were seen in the Nyquist plots, with a spike in the lower-frequency

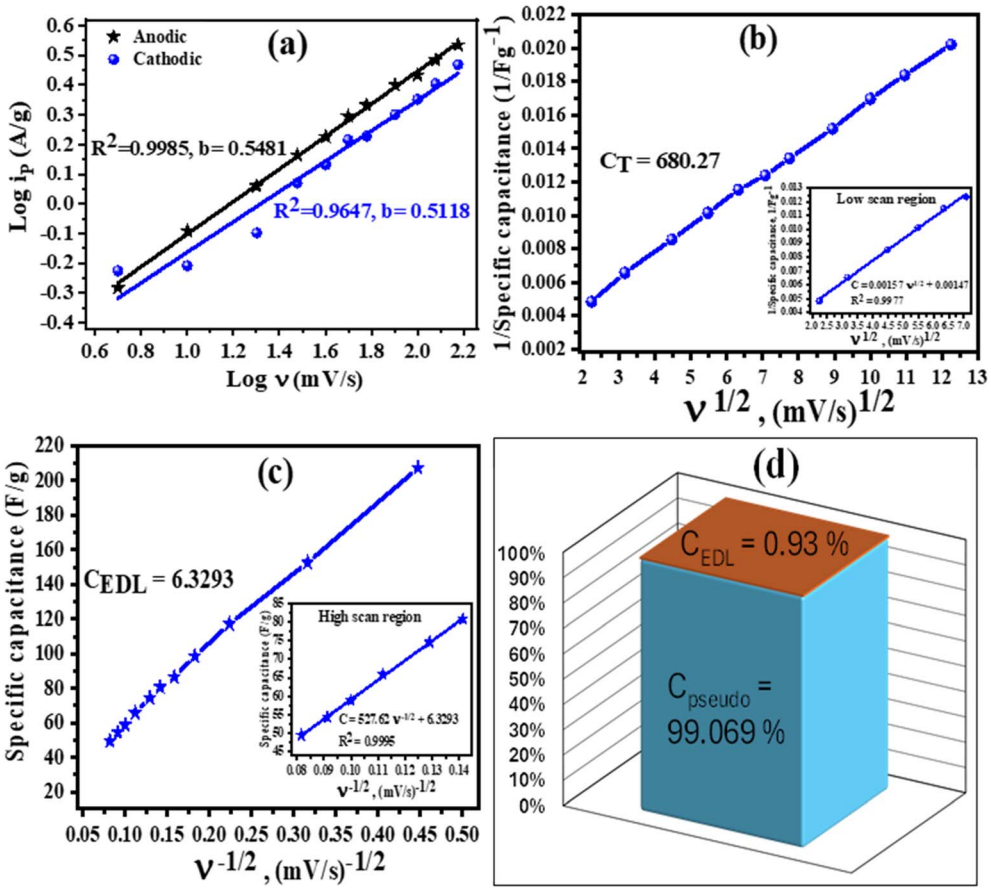

Fig. 8 (a) Linear plot of logarithmic relationship between the anodic/cathodic peak current density (log i_p) and scan rates (log ν) for the $Ni_{10}Fe_1$-BDC MOF//$Ni_{10}Fe_1$-BDC MOF symmetric cell, (b) plot of the inverse of specific capacitance (C^{-1}) *versus* the square root of the scan rate ($\nu^{1/2}$); inset is the linear plot of the low scan-rate region, (c) plot of specific capacitance (C) *versus* the inverse of the square root of the scan rate ($\nu^{-1/2}$); inset is the linear plot of the high scan-rate region, and (d) contributions of electric double-layer capacitance and pseudocapacitance to the $Ni_{10}Fe_1$-BDC MOF//$Ni_{10}Fe_1$-BDC MOF symmetric cell's total capacitance.

area. The spike corresponds to the transport of electrolyte ions to the electrode surface (Warburg resistance, W_o). In addition, the straight line in Z_{im}, which is ascribed to capacitive behavior, was obvious for all studied electrodes. Furthermore, the internal resistance of the electrochemical system (R_s), which comprises the intrinsic resistance of the electroactive material, electrolyte resistance, and contact resistance of the electrode/electrolyte interface, is designated by the intersection with the real axis in the high-frequency region. Additionally, in the high-frequency region, all the electrodes showed non-obvious semi-circles, which signify quick electron transport kinetics and insignificant charge transfer resistance at the electrode/electrolyte interface.[47] The parameters calculated from EC are presented in Table S2. As seen in Fig. 5f and Table S2, the $Ni_{10}Fe_1$-BDC MOF electrode showed a vertical line inclined more to the imaginary axis as well as lower values for R_s, R_{ct} and W than the other electrodes, indicating less resistance, high electrical conductivity, fast rates of electron transfer and ion diffusion at the electrode/electrolyte interface, which contribute to improving the supercapacitor electrochemical performance.

3.2.2. Two-electrode electrochemical performance study (symmetric supercapacitor). To investigate the practical applicability of the $Ni_{10}Fe_1$-BDC MOF electrode, a symmetric supercapacitor cell (SSC) was tested using 1 M KOH as the electrolyte. The electrodes were fabricated using $Ni_{10}Fe_1$-BDC MOF material. Since the electrodes were symmetric, there was no need to balance the charges. Firstly, the potential window was studied, similar to the three-electrode system, from −0.4 to 0.6 V, as shown in Fig. S4. However, the obtained capacitance was very low, and therefore, the potential range was varied from 1 to 2 V by checking the CV curves at 50 mV s^{-1} scan rate, as displayed in Fig. 6a. The curves showed leaf-like shapes with a redox peak. The progressive elevation of the maximum current as the maximum voltage increased may be due to the redox processes occurring at the positive and negative electrodes. The CV curves retained their leaf-like shapes, with a redox peak even at 2 V; hence, the potential window was enlarged to 2 V (optimum maximum potential of the SSC was 2 V), which resulted in an excellent improvement in capacitance and hence energy density, as presented in Fig. 6b. The specific capacitance (C_s) increased from 43.82 F g^{-1} at the 1 V potential window to 73.51 F g^{-1} at the 2 V potential window, leading to an energy density 6.71 times higher than that at the 1 V potential window due to the direct relationship between them ($E = CV^2/7.2$).

Fig. 6c shows the CV curves of the $Ni_{10}Fe_1$-BDC MOF//$Ni_{10}Fe_1$-BDC MOF symmetric cell at different sweep rates and fixed potential windows from 0 to 2 V. The curves retained leaf-like shapes, with a redox peak even at a longer scan sweep, indicating a reliable electrochemical behavior and the reversibility of the system. Furthermore, the current density improved with increasing sweep rates due to the speedy movement of electrolyte ions at high scan rates. The graphs in Fig. 6d display the GCD curves under different current densities of 1, 2, 3, 4, 5, 6, 8, 10, 12, and 15 A g^{-1}. The curves display linear non-triangular shapes. The excellent coulombic efficiency and optimal capacitive characteristics of the electrodes are confirmed by the symmetrical curves. The specific capacitances (C_s) and capacities (Q_s) were calculated at various current densities using eqn (7) or (8) and (9), respectively, and are displayed in Fig. 6e. The obtained value of capacitance (C_s) was 221.48 F g^{-1} (411.96 C per g capacity) at a current density of 1 A g^{-1} and 21.36 F g^{-1} (28.2 C per g capacity) at 15 A g^{-1}. Besides, the energy density (E_d) and power density (P_d) were calculated using eqn (10) and (11), respectively. Moreover, the symmetric cell displayed a robust E_d of 106.42 Wh kg^{-1} at a P_d of 3720 W kg^{-1} and 1 A g^{-1}, while demonstrating a P_d of 39 600 W kg^{-1} at 5.17 Wh kg^{-1} E_d and 15 A g^{-1}. Fig. 6f demonstrates the relationship of E_d and P_d of the symmetric supercapacitor with current density. The energy density decreased as the current density increased, along with increasing the power density.

For supercapacitor applications, cycling capability is crucial. The capacitance retention of the SSC was investigated by using the GCD technique at 8 A g^{-1} current density for 2000 consecutive charge/discharge cycles (Fig. 7a). The capacitance progressively increased until 137.73% of its original capacitance was accomplished after 2000 cycles, perhaps because of the active site exposure to the electrolyte ions leading to the activation of the electrode through gradual penetration of the electrolyte deeply through the pores, indicating the good stability of the electrodes. In addition, 78.01% of the initial coulombic efficiency was retained after 2000 GCD cycles. Furthermore, a comparison of the first and last five cycles of the entire cycling test is shown in Fig. 7b. The figures do not reveal any distinct changes in shape, verifying the stability of the electrodes. Furthermore, the last five cycles consumed more time than the first ones, confirming the improvement in performance and the good stability of the symmetric supercapacitor cell. To acquire additional information about the electrochemical properties, EIS measurements of the $Ni_{10}Fe_1$-BDC MOF//$Ni_{10}Fe_1$-BDC MOF symmetric cell were further performed prior to and after the stability test, as presented in Fig. 7c. The electrochemical equivalent circuit (EC) used to fit the experimental data was the same one used for the three-electrode system. The Nyquist plots prior to and after 2000 cycles of charge and discharge (GCD) had the same shapes, with very slight variation in the values of EC parameters, suggesting the good cycling stability of the $Ni_{10}Fe_1$-BDC MOF//$Ni_{10}Fe_1$-BDC MOF symmetric cell. The R_s value increased from 4.982 Ω to 6.490 Ω, and charge transfer resistance (R_{ct}) increased from 102.5 Ω to 120.7 Ω for R_{ct1} and from 3.937 Ω to 13.61 Ω for R_{ct2}, which can result from the accumulation of electrolyte ions.

As displayed in the Ragone plot, the $Ni_{10}Fe_1$-BDC MOF//$Ni_{10}Fe_1$-BDC MOF symmetric supercapacitor cell displayed an extreme E_d of 106.42 Wh kg^{-1} at 3720 W kg^{-1} P_d. Even when the P_d increased to 39 600 W kg^{-1}, the E_d was maintained at 5.17 Wh kg^{-1} (Fig. 7d). This performance is significantly better than that of many reported symmetric supercapacitors, including Ni–Zn MOF//Ni–Zn MOF SC-SD (33.25 Wh kg^{-1} at 900 W kg^{-1}),[48] MIL(Fe)-C-800//MIL(Fe)-C-800 SSC (1.13 Wh kg^{-1} at 400 W kg^{-1}),[49] $LaFeO_3$ derived from MOF SSC (34 Wh kg^{-1} at 900 W kg^{-1}),[50] Co_3O_4/Fe_2O_3//Co_3O_4/Fe_2O_3 derived from MOF SSC (35.15 Wh kg^{-1} at 1125 W kg^{-1}),[51] Mn/Ni-MOF@MWCNTs//Mn/Ni-MOF@MWCNTs SSC (33.2 Wh kg^{-1} at 1198 W kg^{-1})[52] and $NiFe_2O_4$//$NiFe_2O_4$ symmetric supercapacitor (47 Wh kg^{-1} at 333 W kg^{-1}).[53]

The charge storage mechanism of the $Ni_{10}Fe_1$-BDC MOF//$Ni_{10}Fe_1$-BDC MOF symmetric cell was analyzed using eqn (17) by plotting $\log i_p$ *versus* log scan rate ($\log \nu$) for both anodic and cathodic currents, as shown in Fig. 8a. The *b* values derived from the anodic and cathodic currents were clearly between 0.5 and 1 (0.5481 for the anodic current and 0.5118 for the cathodic current), proving that charge storage occurs through both surface-controlled processes (contributed by electric-double layer capacitance) and diffusion-controlled processes; besides, the predominant behaviour was pseudocapacitance. Additionally, the Trasatti method was employed to more clearly determine the quantitative analysis of charge distribution and the percentage contributions of both pseudocapacitance (C_{PC}) and electric double-layer capacitance (C_{EDL}) to the overall specific capacitance. The relationship between the change in total capacitance (C_T) and scan rate (ν) in this approach is as follows:[54,55]

$$\frac{1}{C} = K_1\sqrt{\nu} + \frac{1}{C_T} \tag{18}$$

$$C = K_2\frac{1}{\sqrt{\nu}} + C_{EDL} \tag{19}$$

where K_1 and K_2 are arbitrary constants. First, the inverse of the specific capacitance (C^{-1}) was plotted against the square root of scan rate ($\sqrt{\nu}$), as illustrated in Fig. 8b. The total specific capacitance (C_T) of electrode materials was determined from the inverse of the *y*-intercept by extending the linearly fitted line in the low scan-rate region, according to eqn (18). In addition, C_{EDL} was computed by plotting the specific capacitance (C) against the inverse square root of the scan rate ($1/\sqrt{\nu}$), as presented in Fig. 8c. The C_{EDL} of the electrode material was obtained from the *y*-intercept by extending the linearly fitted line in the high scan-rate region ($\nu \to \infty$), according to eqn (19). Furthermore, the pseudocapacitance (C_{pseudo}) values of the electrode materials were calculated by subtracting the electrical double layer capacitance (C_{EDL}) from the total capacitance (C_T). As demonstrated in Fig. 8b and c, the values of C_T, C_{EDL}, and C_{pseudo} were estimated as 680.27, 6.3293, and 673.94, respectively. The percentage contribution of pseudocapacitance (C_{pseudo}) and electrical double layer capacitance (C_{EDL}) in the $Ni_{10}Fe_1$-BDC MOF//$Ni_{10}Fe_1$-BDC MOF symmetric cell is shown in Fig. 8d. Therefore, the ratio of pseudocapacitance was

obtained as about 99.069% while that of C_{EDL} was only 0.93% with respect to total capacitance (C_T).

4 Conclusion

In brief, we synthesized monometallic (Fe-BDC MOF) and bimetallic (NiFe-BDC MOFs) metal–organic frameworks with varying molar ratios and morphologies using a solvothermal method and investigated them as supercapacitor electrode materials. According to the SEM results, the NiFe-BDC MOFs were smaller than the Fe-BDC MOF particles, with an improvement in the number of electroactive sites and electrolyte ion movement through the electrode. The synthesis of the Fe-BDC MOF and NiFe-BDC MOFs was successfully verified by the XRD data. The specific surface area of $Ni_{10}Fe_1$-BDC MOF was further calculated by BET analysis as 2.2965 $m^2\ g^{-1}$, with an adsorption-averaged pore radius of 258.2522 Å. The electrochemical characteristics of the prepared materials were assessed through the application of CV, GCD, and EIS methodologies. A maximum specific capacitance of 918.75 F g^{-1} was achieved for the $Ni_{10}Fe_1$-BDC MOF electrode, while 196.24 F g^{-1} was achieved for the Fe-BDC MOF electrode at 4 A g^{-1} current density. The $Ni_{10}Fe_1$-BDC MOF electrode demonstrated capacitance retention of 72.22% after 2000 GCD cycles at 12 A g^{-1} compared with 36.88% for the Fe-BDC MOF electrode. The EIS analysis proved the higher electrochemical performance of the $Ni_{10}Fe_1$-BDC MOF electrode than that of other samples based on the low values of Warburg resistance and charge-transfer resistance (4.076 Ω) between the interface of the electrode and the electrolyte. The symmetric supercapacitor (SSC) composed of $Ni_{10}Fe_1$-BDC MOF electrodes exhibited a 2 V potential window, a maximum energy density of 106.42 Wh kg^{-1} at a 3720 W kg^{-1} power density, a 137.73% capacitance retention, and 78.01% coulombic efficiency after 2000 charge/discharge cycles. The outcomes indicate that the $Ni_{10}Fe_1$-BDC MOF is a suitable high-performance electrode material for supercapacitor applications.

Conflicts of interest

There are no conflicts to declare.

Data availability

All data underlying the results are available as part of the article and no additional source data are required.

Supplementary information (SI) is available. See DOI: https://doi.org/10.1039/d5na00246j.

References

1 H. Zhou, H. Cao, Y. Qu and Y. Wang, Self-supporting Co-MoOx@N-doped carbon/expanded graphite paper for efficient water splitting catalyst, *Diam. Relat. Mater.*, 2023, **140**, 110501, DOI: 10.1016/j.diamond.2023.110501.

2 Y. Liu, S. Li, C. Wang, L. Guo and Y. Wang, Accordion-like bimetal-organic framework anchoring on the partially-exfoliated graphite paper for high-performance supercapacitors, *Appl. Surf. Sci.*, 2020, **528**, 146954, DOI: 10.1016/j.apsusc.2020.146954.

3 R. R. Ikreedeegh, S. Tasleem and M. A. Hossen, Facile fabrication of binary g-C3N4/NH2-MIL-125(Ti) MOF nanocomposite with Z-scheme heterojunction for efficient photocatalytic H2 production and CO2 reduction under visible light, *Fuel*, 2024, **360**, 130561, DOI: 10.1016/j.fuel.2023.130561.

4 S. Weng, Q. An, Y. Xu, Y. Jiao and J. Chen, In-Situ Formation of NiFe-MOF on Nickel Foam as a Self-Supporting Electrode for Flexible Electrochemical Sensing and Energy Conversion, *Chemosensors*, 2023, **11**(4), 242, DOI: 10.3390/chemosensors11040242.

5 J. Zhao, L. Yang, R. Li and Y. Zhou, One−Step Synthesis of Fe−Based Metal–Organic Framework (MOF) Nanosheet Array as Efficient Cathode for Hybrid Supercapacitors, *Inorganics*, 2023, **11**(4), 169, DOI: 10.3390/inorganics11040169.

6 D. Yu, Q. Shao, Q. Song, J. Cui, Y. Zhang, B. Wu, L. Ge, Y. Wang, Y. Zhang, Y. Qin, R. Vajtai, P. M. Ajayan, H. Wang, T. Xu and Y. Wu, A solvent-assisted ligand exchange approach enables metal-organic frameworks with diverse and complex architectures, *Nat. Commun.*, 2020, **11**, 927, DOI: 10.1038/s41467-020-14671-9.

7 P. Du, Y. Dong, C. Liu, W. Wei, D. Liu and P. Liu, Fabrication of hierarchical porous nickel based metal-organic framework (Ni-MOF) constructed with nanosheets as novel pseudo-capacitive material for asymmetric supercapacitor, *J. Colloid Interface Sci.*, 2018, **518**, 57–68, DOI: 10.1016/j.jcis.2018.02.010.

8 M. Rinawati, Y. X. Wang, K. Y. Chen and M. H. Yeh, Designing a spontaneously deriving NiFe-LDH from bimetallic MOF-74 as an electrocatalyst for oxygen evolution reaction in alkaline solution, *Chem. Eng. J.*, 2021, **423**, 130204, DOI: 10.1016/j.cej.2021.130204.

9 T. Kumar, B. Devi, A. Halder and R. R. Koner, NiFe-Coordination Polymers-Derived Layered Double Hydroxides as Bifunctional Materials: Effect of the Ni: Fe Ratio on the Electrochemical Performance, *ChemPlusChem*, 2023, **88**(8), DOI: 10.1002/cplu.202300186.

10 Y. Zhao, Y. Chen, Q. Liu, M. Yuan, Y. Huang, J. Lian, J. Bao, J. Qiu, H. Xu, Y. Xu and H. Li, Construction of cobaltous oxide/nickel–iron oxide electrodes with great cycle stability and high energy density for advanced asymmetry supercapacitor, *J. Mater. Sci. Mater. Electron.*, 2019, **30**, 21219–21228, DOI: 10.1007/s10854-019-02495-3.

11 J. Choi, A. Nkhama, A. Kumar, S. R. Mishra, F. Perez and R. K. Gupta, A facile preparation of sulfur doped nickel–iron nanostructures with improved HER and supercapacitor performance, *Int. J. Hydrogen Energy*, 2022, **47**, 7511–7521, DOI: 10.1016/j.ijhydene.2021.12.117.

12 W. Dong, Z. Liu, H. Sun, Z. Shi and J. Xu, Ultrathin defect-rich nanosheets of NiFe-MOF with high specific capacitance and stability for supercapacitor, *Mater. Today Chem.*, 2024, **36**, 101938, DOI: 10.1016/j.mtchem.2024.101938.

13 R. Nivetha, J. Jana, S. Ravichandran, H. N. Diem, T. Van Phuc, J. S. Chung, S. G. Kang, W. M. Choi and S. H. Hur, Two-dimensional bimetallic Fe/M- (Ni, Zn, Co and Cu) metal organic framework as efficient and stable electrodes for overall water splitting and supercapacitor applications, *J. Energy Storage*, 2023, **61**, 106702, DOI: 10.1016/j.est.2023.106702.

14 X. Zhang, Q. Yin, F. Cao, Y. Wang, N. Liu, J. Liu and R. Liu, Synthesis of NiFe-MOF@NiFeTe nanoparticle-rod heterostructure on nickel foam for high-performance hybrid supercapacitors, *Appl. Surf. Sci.*, 2023, **616**, 156533, DOI: 10.1016/j.apsusc.2023.156533.

15 P. D. Patil, S. R. Shingte, V. C. Karade, J. H. Kim, T. D. Dongale, S. H. Mujawar, A. M. Patil and P. B. Patil, Effect of annealing temperature on morphologies of metal organic framework derived NiFe2O4 for supercapacitor application, *J. Energy Storage*, 2021, **40**, 102821, DOI: 10.1016/j.est.2021.102821.

16 Y. Zhang, J. Zhang, H. Li, H. Yao and X. Wang, Influence of different Ni:Fe molar ratios on the properties of NiFe-LDH as electrode materials for supercapacitor applications, *Int. J. Electrochem. Sci.*, 2024, **19**, 100590, DOI: 10.1016/j.ijoes.2024.100590.

17 K. Chhetri, T. Kim, D. Acharya, A. Muthurasu, B. Dahal, R. M. Bhattarai, P. C. Lohani, I. Pathak, S. Ji, T. H. Ko and H. Y. Kim, Hollow Carbon Nanofibers with Inside-outside Decoration of Bi-metallic MOF Derived Ni-Fe Phosphides as Electrode Materials for Asymmetric Supercapacitors, *Chem. Eng. J.*, 2022, **450**, 138363, DOI: 10.1016/j.cej.2022.138363.

18 R. Xin, M. Kim, P. Cheng, A. Ashok, S. Chowdhury, T. Park, A. Alowasheeir, M. S. Hossain, J. Tang, J. W. Yi, Y. Yamauchi, Y. V. Kaneti and J. Na, Enlarging the porosity of metal-organic framework-derived carbons for supercapacitor applications by a template-free ethylene glycol etching method, *J. Mater. Chem. A*, 2022, **11**, 12759–12769, DOI: 10.1039/d2ta06307g.

19 M. Anwar, E. W. Cochran, S. Zulfiqar, M. F. Warsi, I. Shakir and K. Chaudhary, In-situ fabricated copper-holmium co-doped cobalt ferrite nanocomposite with cross-linked graphene as novel electrode material for supercapacitor application, *J. Energy Storage*, 2023, **72**, 108438, DOI: 10.1016/j.est.2023.108438.

20 M. R. Biradar, A. V. Salkar, P. P. Morajkar, S. V. Bhosale and S. V. Bhosale, Designing neurotransmitter dopamine-functionalized naphthalene diimide molecular architectures for high-performance organic supercapacitor electrode materials, *New J. Chem.*, 2021, **45**, 9346–9357, DOI: 10.1039/d1nj00269d.

21 M. R. Pallavolu, S. A. Thomas, J. Cherusseri, B. A. Al-Asbahi, H. T. Das, S. Adem and S. W. Joo, Scalable synthesis of binder-free hierarchical MnCo2O4 nanospikes/Ni(OH)2 nanosheets composite electrodes for high-capacity supercapatteries, *J. Energy Storage*, 2023, **73**, 108999, DOI: 10.1016/j.est.2023.108999.

22 J. Xing, J. Du, X. Zhang, Y. Shao, T. Zhang and C. Xu, Ni-P@NiCo LDH core-shell nanorod-decorated nickel foam with enhanced areal specific capacitance for high-performance supercapacitors, *Dalton Trans.*, 2017, **46**, 10064–10072, DOI: 10.1039/c7dt01910f.

23 S. A. Melchior, K. Raju, I. S. Ike, R. M. Erasmus, G. Kabongo, I. Sigalas, S. E. Iyuke and K. I. Ozoemena, High-Voltage Symmetric Supercapacitor Based on 2D Titanium Carbide (MXene, Ti 2 CT x)/Carbon Nanosphere Composites in a Neutral Aqueous Electrolyte, *J. Electrochem. Soc.*, 2018, **165**, A501–A511, DOI: 10.1149/2.0401803jes.

24 S. Khamlich, Z. Abdullaeva, J. V. Kennedy and M. Maaza, High performance symmetric supercapacitor based on zinc hydroxychloride nanosheets and 3D graphene-nickel foam composite, *Appl. Surf. Sci.*, 2017, **405**, 329–336, DOI: 10.1016/j.apsusc.2017.02.095.

25 G. Liu, Y. Shi, L. Wang, Y. Song, S. Gao, D. Liu and L. Fan, Reduced graphene oxide/polypyrrole composite: an advanced electrode for high-performance symmetric/asymmetric supercapacitor, *Carbon Lett.*, 2020, **30**, 389–397, DOI: 10.1007/s42823-019-00108-x.

26 S. Ur Rahman, P. Röse, A. Ul Haq Ali Shah, U. Krewer, S. Bilal and S. Farooq, Exploring the functional properties of sodium phytate doped polyaniline nanofibers modified fto electrodes for high-performance binder free symmetric supercapacitors, *Polymers*, 2021, **13**(14), 2329, DOI: 10.3390/polym13142329.

27 Z. Song, D. Zhu, L. Li, T. Chen, H. Duan, Z. Wang, Y. Lv, W. Xiong, M. Liu and L. Gan, Ultrahigh energy density of a N, O codoped carbon nanosphere based all-solid-state symmetric supercapacitor, *J. Mater. Chem. A*, 2019, **7**, 1177–1186, DOI: 10.1039/c8ta10158b.

28 W. H. Low, P. S. Khiew, S. S. Lim, C. W. Siong, C. H. Chia and E. R. Ezeigwe, Facile synthesis of graphene-Zn3V2O8 nanocomposite as a high performance electrode material for symmetric supercapacitor, *J. Alloys Compd.*, 2019, **784**, 847–858, DOI: 10.1016/j.jallcom.2019.01.137.

29 M. Alaide de Oliveira, E. Silva Souza, J. de Jesus Santana, N. Łukasik, B. Stefany Lima da Silva, B. Silva Barros and J. Kulesza, M-BDC (M = Co and/or Fe) MOFs as effective catalysts for hydrogen generation via hydrolysis of sodium borohydride, *Appl. Surf. Sci.*, 2023, **628**, 157361, DOI: 10.1016/j.apsusc.2023.157361.

30 C. Ajpi, N. Leiva, A. Lundblad, G. Lindbergh and S. Cabrera, Synthesis and spectroscopic characterization of Fe3+-BDC metal organic framework as material for lithium ion batteries, *J. Mol. Struct.*, 2023, **1272**, 134127, DOI: 10.1016/j.molstruc.2022.134127.

31 O. Abuzalat, D. Wong and M. A. Elsayed, Nano-Porous Composites of Activated Carbon–Metal Organic Frameworks (Fe-BDC@AC) for Rapid Removal of Cr (VI): Synthesis, Adsorption, Mechanism, and Kinetics Studies, *J. Inorg. Organomet. Polym. Mater.*, 2022, **32**, 1924–1934, DOI: 10.1007/s10904-022-02237-9.

32 A. S. Rajpurohit, D. K. Bora and A. K. Srivastava, Simultaneous determination of amlodipine and losartan using an iron metal-organic framework/mesoporous carbon nanocomposite-modified glassy carbon electrode by

differential pulse voltammetry, *Anal. Methods*, 2018, **10**, 5423–5438, DOI: 10.1039/c8ay01553h.

33 M. Zainuri, Hematite from Natural Iron Stones as Microwave Absorbing Material on X-Band Frequency Ranges, *IOP Conf. Ser. Mater. Sci. Eng.*, 2017, **196**, 012008, DOI: 10.1088/1757-899X/196/1/012008.

34 M. Chirita, M. L. Kiss, A. Ieta, A. Ercuta and I. Grozescu, Synthesis of micrometric single crystalline magnetite with superparamagnetic properties for biomedical applications, *Tech. Proc. 2013 NSTI Nanotechnol. Conf. Expo, NSTI-Nanotech*, 2013, vol. 1, pp. 378–381.

35 J. Li, S. Ma, Z. Qi, J. Ding, M. Yin, B. Zhao, Z. Zhang, Y. Wang, H. Zhang, L. Wang and D. D. Dionysiou, Insights into the removal of chloramphenicol by electrochemical reduction on Pd/NiFe-MOF/foam-Ni electrode: performance and mechanism, *Appl. Catal., B*, 2023, **322**, 122076, DOI: 10.1016/j.apcatb.2022.122076.

36 J. Yang, P. Xiong, C. Zheng, H. Qiu and M. Wei, Metal–organic frameworks: a new promising class of material for high performance supercapacitor electrode, *J. Mater. Chem. A*, 2014, **2**, 16640–16644, DOI: 10.1039/C4TA04140B.

37 Q. Yin, T. Xu, F. Cao, Y. Wang, C. Yang, N. Liu, J. Liu and R. Liu, Heterostructures of NiFe-MOF/PBAs with high-performance supercapacitors obtained by compounding Prussian blue analogues on bimetallic organic frames, *Electrochim. Acta*, 2024, **476**, 143749, DOI: 10.1016/j.electacta.2023.143749.

38 Z. Yan, H. Qi, X. Bai, K. Huang, Y. R. Chen and Q. Wang, Mn doping of cobalt oxynitride coupled with N-rGO nanosheets hybrid as a highly efficient electrocatalyst for oxygen reduction and oxygen evolution reaction, *Electrochim. Acta*, 2018, **283**, 548–559, DOI: 10.1016/j.electacta.2018.06.185.

39 M. Gupta, S. Tyagi and N. Kumari, Electrochemical performance of hybrid spinel ferrite/carbon (NiFe2O4/C) nanocomposite derived from metal organic frameworks (MOF) as electrode material for supercapacitor application, *J. Solid State Electrochem.*, 2024, **28**, 169–180, DOI: 10.1007/s10008-023-05665-w.

40 Z. Jiao, Y. Chen, M. Du, M. Demir, F. Yan, W. Xia, Y. Zhang, C. Wang, M. Gu, X. Zhang and J. Zou, 3D hollow NiCo LDH nanocages anchored on 3D CoO sea urchin-like microspheres: a novel 3D/3D structure for hybrid supercapacitor electrodes, *J. Colloid Interface Sci.*, 2023, **633**, 723–736, DOI: 10.1016/j.jcis.2022.11.131.

41 X. Wei, S. Su and Q. Zhang, Construction of Hierarchical NiCoP NiFe-LDH Nanoflakes Heterostructure for High Energy Asymmetric Supercapacitor, *ChemElectroChem*, 2023, **10**(11), 202201166.

42 Z. Cui, F. Yi, T. Meng, A. Gao, J. Hao, Y. Wang, S. Li, J. Huang and D. Shu, Advanced hollow structure with functional Interface of NiCoP/NC achieved superior hydroxide ion storage for high-rate supercapacitor, *Sustain. Mater. Technol.*, 2023, **37**, e00678, DOI: 10.1016/j.susmat.2023.e00678.

43 Q. A. Sial, S. S. Kalanur and H. Seo, Lamellar flower inspired hierarchical alpha manganese vanadate microflowers for high-performance flexible hybrid supercapacitors, *Ceram. Int.*, 2022, **48**, 24989–24999, DOI: 10.1016/j.ceramint.2022.05.152.

44 Y. Seo, P. A. Shinde, S. Park and S. C. Jun, Self-assembled bimetallic cobalt–manganese metal–organic framework as a highly efficient, robust electrode for asymmetric supercapacitors, *Electrochim. Acta*, 2020, **335**, 135327, DOI: 10.1016/j.electacta.2019.135327.

45 D. Acharya, I. Pathak, B. Dahal, P. C. Lohani, R. M. Bhattarai, A. Muthurasu, T. Kim, T. H. Ko, K. Chhetri and H. Y. Kim, Immoderate nanoarchitectures of bimetallic MOF derived Ni–Fe–O/NPC on porous carbon nanofibers as freestanding electrode for asymmetric supercapacitors, *Carbon*, 2023, **201**, 12–23, DOI: 10.1016/j.carbon.2022.08.091.

46 M. Moradi, A. Afkhami, T. Madrakian and H. R. Moazami, Electrosynthesis of Co–Mn layered-double-hydroxide as a precursor for Co-Mn-MOFs and subsequent electrochemical sulfurization for supercapacitor application, *J. Energy Storage*, 2023, **71**, 108177, DOI: 10.1016/j.est.2023.108177.

47 S. Daneshvar and M. Arvand, In-situ growth of hierarchical Ni–Co LDH/CoMoO4 nanosheets arrays on Ni foam for pseudocapacitors with robust cycle stability, *J. Alloys Compd.*, 2020, **815**, 152421, DOI: 10.1016/j.jallcom.2019.152421.

48 J. Zeng, K. C. Devarayapalli, S. V. P. Vattikuti and J. Shim, Split-cell symmetric supercapacitor performance of bimetallic MOFs yolk-shell hierarchical microstructure, *Mater. Lett.*, 2022, **309**, 131305, DOI: 10.1016/j.matlet.2021.131305.

49 Y. F. Wu, T. R. Kuo, L. Y. Lin, S. Kubendhiran, K. C. Lai, T. Y. Chen and S. Yougbaré, Investigating energy storage ability of MIL101-(Fe) derivatives prepared using successive carbonization and oxidation for supercapacitors, *J. Energy Storage*, 2022, **55**(part A), 105420, DOI: 10.1016/j.est.2022.105420.

50 Y. Zhang, J. Ding, W. Xu, M. Wang, R. Shao, Y. Sun and B. Lin, Mesoporous LaFeO3 perovskite derived from MOF gel for all-solid-state symmetric supercapacitors, *Chem. Eng. J.*, 2020, **386**, 124030, DOI: 10.1016/j.cej.2020.124030.

51 X. Wei, Y. Li, H. Peng, D. Gao, Y. Ou, Y. Yang, J. Hu, Y. Zhang and P. Xiao, A novel functional material of Co3O4/Fe2O3 nanocubes derived from a MOF precursor for high-performance electrochemical energy storage and conversion application, *Chem. Eng. J.*, 2019, **355**, 336–340, DOI: 10.1016/j.cej.2018.08.009.

52 Y. Han, J. Zhou, L. Wang, L. Xing, Z. Xue, Y. Jiao and Y. Pang, Redox-active nanostructure electrode of Mn/Ni bimetal organic frameworks anchoring on multi-walled carbon nanotubes for advanced supercapacitor, *J. Electroanal. Chem.*, 2021, **882**, 114993, DOI: 10.1016/j.jelechem.2021.114993.

53 S. B. Bandgar, M. M. Vadiyar, Y. C. Ling, J. Y. Chang, S. H. Han, A. V. Ghule and S. S. Kolekar, Metal Precursor Dependent Synthesis of NiFe2O4 Thin Films for High-Performance Flexible Symmetric Supercapacitor, *ACS Appl. Energy Mater.*, 2018, **1**, 638–648, DOI: 10.1021/acsaem.7b00163.

54 A. Asghari, S. Dalvand, M. s. Miresmaeili, F. Khoramjah, M. Omidvar, M. Kambarani and N. Mohammadi, Reactive Red 198 as high-performance redox electrolyte additive for defective mesoporous carbon-based supercapacitor, *Int. J. Hydrogen Energy*, 2023, **48**, 9776–9784, DOI: 10.1016/j.ijhydene.2022.11.322.

55 S. Ansari, R. B. Choudhary and A. Gupta, Nanoflower copper sulphide intercalated reduced graphene oxide integrated polypyrrole nano matrix as robust symmetric supercapacitor electrode material, *J. Energy Storage*, 2023, **59**, 106446, DOI: 10.1016/j.est.2022.106446.